EEET ECOLOGICAL ENGINEERING & ENVIRONMENTAL TECHNOLOGY

Ecological Engineering & Environmental Technology 2024, 25(1), 164–179
https://doi.org/10.12912/27197050/174738
ISSN 2719-7050, License CC-BY 4.0

Received: 2023.10.18
Accepted: 2023.11.21
Published: 2023.12.14

Mapping Soil Clay Content and Hydraulic Properties over an Agricultural Semiarid Plain Using Remote Sensing and Interpolation Techniques

Houda Nassah[1], Fakir Younes[2,3], Erraki Salah[3,4], Khabba Said[5,3], Mougenot Bernard[5,6]

[1] Department of Health and Agro-Industry Engineering High School of Engineering and Innovation of Marrakesh, Private University of Marrakesh, Road Amezmiz, Marrakech, Morocco
[2] LMI TREMA, Cadi Ayyad University, Marrakech, Morocco
[3] Center for Remote Sensing Applications, Mohammed VI Polytechnic University, Morocco
[4] Faculty of Science and Technology, University Cadi Ayyad, Marrakech, Morocco
[5] Department of Physics, Faculty of Science Semlalia, University Cadi Ayyad, Marrakech, Morocco
[6] Centre d'Etudes Spatiales de la Biosphère, 31400 Toulouse, France
* Corresponding author's e-mail: houda.nassah@gmail.com

ABSTRACT

Clay content is an important parameter governing hydrodynamics property of soils and consequently crucial to environmental management and agricultural development. The present study aims to use the textural middle infrared index (MID index) product of Landsat-8 Operational Land Images to map clay content over the Haouz plain (Central Morocco). The clay content was mapped at 30 m grid spatial resolution based on the relationship between the MID index and a large set of soil samples. Over the areas covered by green vegetation, the clay content was predicted using the ordinary cokriging technique. Then, this information was used to derive soil hydraulic properties such as the field capacity (θ_{fc}), the wilting point (θ_{wp}) and the saturated hydraulic conductivity (K_{sat}) by using different pedotransfer functions. The validation of the maps was performed by using independent soil samples and measurements. The results showed that the clay content is significantly correlated to MID index. The ordinary cokriging improved mapping of clay content over the Haouz plain ($R^2 = 0.70$, RMSE = 3.5%). The obtained maps of θ_{fc}, θ_{wp} and K_{sat} revealed a good correlation between the simulated values and the measured values.

Keywords: topsoil clay content; MID-infrared index; Landsat-8 images; ordinary cokriging; soil hydraulic properties.

INTRODUCTION

Spatial variability of soil characteristics is one of the main requirements of agricultural development and environmental management [Blanco-Canqui and Lal, 2008; Mulder et al., 2011]. Furthermore, several models that address hydrological processes, climate change and land degradation require soil input parameters [Bastiaanssen et al., 2005; Anderson, 2008; Lal and Stewart, 2013]. Soil texture is one of the main characteristics that affect many physical properties [Greve et al., 2012; Wang et al., 2015]. More specifically, the clay content allows predicting soil hydraulic parameters [Shabou et al., 2015].

Mapping the spatial distribution of clay content over large areas using ground measurements is very expensive, time consuming and requires extensive field work [Vidhya Lakshmi et al., 2015; Wang et al., 2015]. During the last decades, the remote sensing methods offer the potential of direct or derived soil properties mapping [Kaihua et al., 2013; Shabou et al., 2015]. Several studies highlighted that the reflectance of bare soils was successfully used to estimate the soil texture and moisture content [Kaihua et al.,

2013]. Clay contents were mapped using hyper spectral data [Ouerghemmi et al. 2011, Gomez et al. 2012), or using the visible and near-infrared spectra (400–2500 nm) [Zeynal et al., 2019]. The latter is based on the significant correlation between the clay content and the soil reflectance [Kaihua et al. 2013] since the presence of clay in the soil enhances the absorption in the domain of 2.2 μm [Shabou et al., 2015]. Because hyperspectral data are not easily available, multispectral data are useful to derive soil surface characteristics from satellites products combining radiometric bands in the visible (0.45–0.69 μm), near-infrared (0.76–0.9 μm) and shortwave infrared (1.55–2.35 μm) spectra [Camacho-Tamayo et al. 2014; Vohland et al. 2014]. Consequently, Landsat Thematic Mapper (TM), Landsat-7 Enhanced Thematic Mapper Plus (ETM+), Landsat-8 Operational Land Imager (OLI) and new satellites as Sentinel-2 from ESA are adequate satellite data sources. The two shortwave infrared bands are particularly interesting to determine clay content using the textural indice middle infrared index (MID-infrared) [Shabou et al., 2015]. This index requires dry bare soil, which makes this method usable in semi-arid conditions where vegetation is generally scarce. When the soil surface is partly covered with dry or green vegetation, the MID index is not applicable. Therefore, interpolation geostatistical methods are needed [Webster and Oliver, 2001; Nielsen and Wendroth, 2003]. Ordinary Cokriging is a powerful technique of interpolation to estimate and predict values at unsampled locations using the sampled locations [Reza et al., 2010]. Recently, soil scientists have used this approach to map soil properties from small to large scales using pedotransfer functions (PTFs) [Kaihua et al., 2013; Zhang shi-Wen et al., 2013; Heuvelink et al., 2016].

Various PTFs have been proposed based on clay and silts contents [Giarola et al., 2002; Oliveira et al., 2002), sand and clay contents [Reichert et al., 2009; Saxton and Rawls, 2006] or clay content as the main variable [Boulet et al., 2009; Merlin el al., 2016]. The PTFs are generally established by multivariate regression based on selected laboratory soil samples or field measurements [Reichert et al; 2009; Boulet et al., 2009].

The main objective of the present work was to map clay content on the topsoil of the Haouz plain in the Central Morocco, using remote sensing techniques, and then convert this information into soil hydraulic properties based on PTFs. The study used Landsat-8 Operational Land Imager (OLI) images and a training soil dataset of 200 samples collected over the area. The approach consists in four steps: (1) studying relationships between the MID index and the measured soil clay content over the plain, (2) applying Ordinary cokriging (OK) as interpolation technique to obtain complete coverage of topsoil clay even in the vegetation zones, (3) validating the resulting map based on independent soil samples sets, (4) using PTFs based only on clay content information to derive the hydraulic conductivity, the field capacity and the wilting point.

MATERIALS AND METHODS

Study area

The Haouz plain is located at the central Morocco, between 7˚2' and 9˚1' W and 31˚5' and 32˚ N. It extends over an area of about 6000 km^2. The plain is limited by the Tensfit Wadi in the north and High-Atlas Mountains in the south (Fig. 1). This region has a semi-arid climate, characterized by low and irregular rainfall (250 mm/year) with rainy season concentrated between November-May, and dry one from May to September [Chehbouni et al., 2012; Khabba et al., 2013]. The Haouz plain encompasses irrigated and rainfed agricultural zones. The major agricultural crops are winter wheat, olive, citrus and apricot. In the rainfed zone, the main crop is wheat [Khabba et al., 2013]. The Haouz plain is filled with alluvial plioquaternary deposits [Boukhari, 2015], mainly constituted by clay, silt, sand, and conglomerate (Fig. 2).

The soil texture map of irrigated areas in Haouz plain (Fig. 3) is obtained by compiling existing soil maps from 1970 to 1990 [Benabdelouahab, 2005]. Nine soil classes of the twelve USDA texture classes are observed in the Haouz plain. The FAO textural classes allow simplifying these classes in three classes: fine, moderate/medium and coarse. The fine class (clay and silty clay) covers the eastern irrigated part (Tassaout) and from the center to the southwest of irrigated zone as shown in (Fig. 3). The moderate texture (loamy and silt loam) covers a large area of these irrigated perimeters in northeast, central and western. Whereas the coarse texture (sandy and loamy sand) appears clearly on the wadis beds of (Ghdat, Zat, Ghmat, Ourika and Rheraya) as well as near the western part of the irrigated area between Ourika and Rheraya wadis.

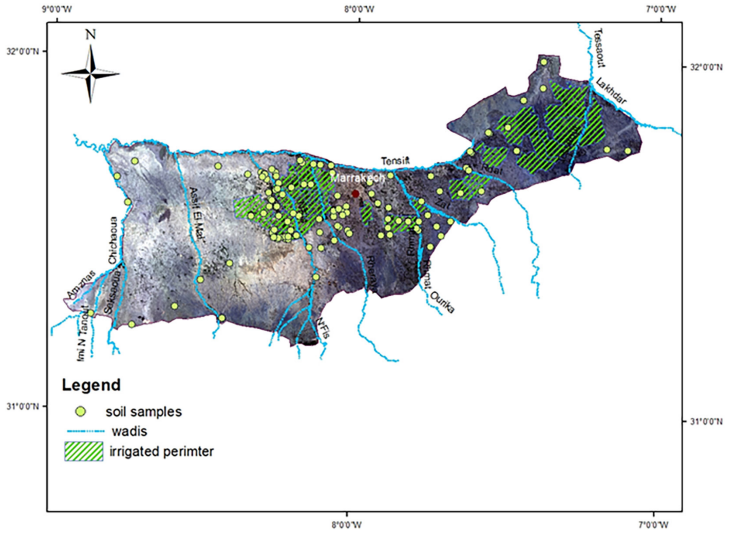

Fig. 1. The Haouz plain, its land use and location of the soil samples

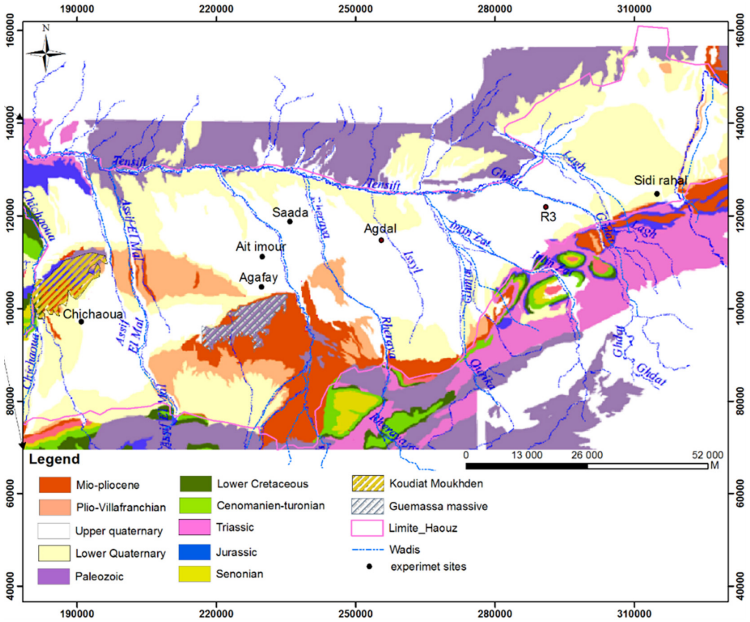

Fig. 2. Geological map of the Haouz plain and its surroundings

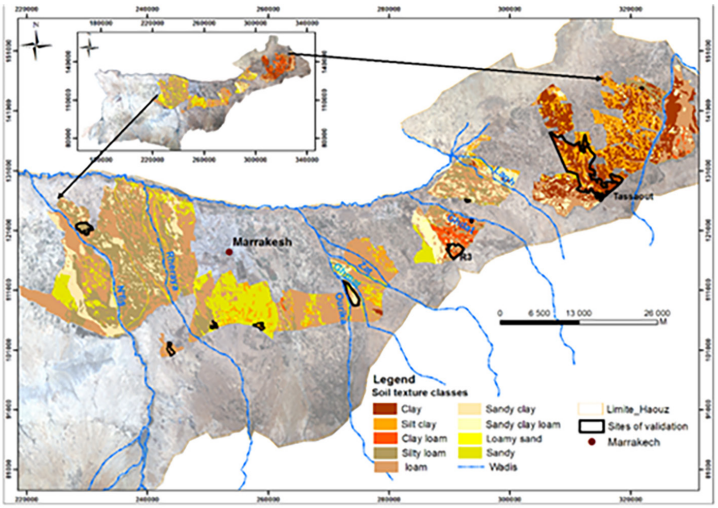

Fig. 3. Soil textures classes in irrigated parts of Haouz plain

Soil sampling and analyses

A total of 200 samples were taken from various pedological formations at the topsoil (0–15 cm); 140 in the agricultural zones and 60 over the bare soil (Fig. 1). The samples were packed in plastic bags and properly marked for identification and analyzes. 20 g of the mixed soil was sampled for analyzing grain size distribution. These soil samples were air-dried and sieved in two fractions: (0.05–2 mm) to calculate the percentage of sand content. While the smaller fraction passed through (0.05 mm) sieve was recovered and collected in vial then analyzed using pipette and/or granulometry laser methods to measure coarse loam (20–50 µm), fine loam (2–20 µm) and clay content (< 2 µm). The soil samples were classified according to the classification system of the USDA, using the Talwin 42 software.

Selection of the appropriate Landsat-8 images

The images download from http://earthexplorer.usgs.gov/ were processed geometrically and atmospherically for 30 m spatial resolution by the MUSCATE software using CNES computing center (add reference for this software). The products are ortho-rectified surface reflectance after atmospheric correction, along with a mask of clouds and their shadows, as well as a mask of water and snow. The atmospheric correction and the cloud detection were processed using the MACCS processor, developed at CESBIO [Hagolle et al., 2010]. The top-of-atmosphere reflectance was converted to surface reflectance then used to calculate normalized difference vegetation index (NDVI) and mid infrared index (MID).

The use of remote sensing for soil studies faces 2 issues: (i) the presence of green or dry vegetation that covers the soil surface [Wang et al., 2015], pixels with green vegetation fraction cover more than 20% and crop residue can prevent direct visualization of bare soil and hamper the soil properties estimation [Bartholomeus et al., 2007]; (ii) the high soil moisture that decreases soil reflectance and increases soil absorption in middle infrared [Muller et Décamps, 2000]. Therefore, to guarantee a maximum of bare soil we selected four images corresponding to dry periods, the dates selected are (22 June 2013, 08 July 2013, 24 July 2013 and 09 August 2013) (Fig. 4).

It was necessary to extract only bare soil zones and apply the MID index to retrieve soil clay fraction. We applied a method proposed by Shabou et al. (2015) in similar conditions in Tunisia. The green vegetation areas for each four selected images were masked based on the NDVI values by applying a threshold of 0.14. To distinguish bare soil from soil with crop residue and agricultural practices, we tested the evolution of the Red band, NDVI and MID-infrared profiles over a field of cereal crop (Fig 3). Based on the Red band time series, we could identify the period of agricultural practices such as plowing period by the decrease in Red band reflectance values [Shabou et al., 2015]. It was possible then to select the period when there is no crop residue by choosing a period that records stable evolution of MID index [Shabou et al., 2015].

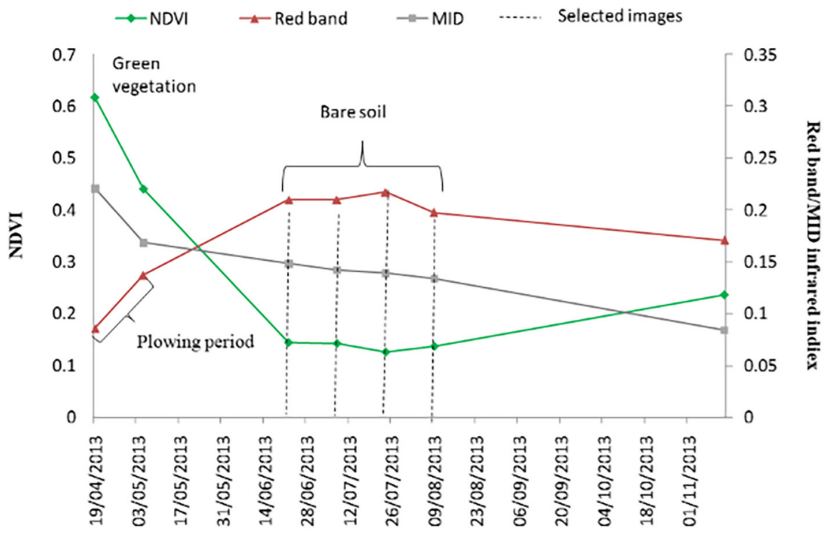

Fig. 4. Evolution of normalized difference vegetation (NDVI), Landsat Red band (TM4) and MID-infrared index ranging from 19 April 2013 until 31 October 2013

The dates at the beginning of the summer season (22 June 2013, 08 July 2013, 24 July 2013 and 09 August 2013) are considered the best period to map a large fraction of bare soil. In the example of the figure 3, red band recorded a stable value of about 0.2. We cannot conclude if the field was ploughed, but the straw coverage is very low with a slight decrease of MID infrareds index. Straw is completely collected by farmers and finally grazed by sheeps.

Afterwards, the pixels corresponding to the 200 soil samples were extracted from the selected Landsat images (22 June 2013, 08 July 2013, 24 July 2013 and 09 August 2013).

Mapping topsoil content over the study area

Over bare soil using the MID index

The MID-infrared index is calculated as Shabou et al. (2015):

$$\text{MID} - \text{Infrared} = \frac{\text{TM6}-\text{TM7}}{\text{TM6}+\text{TM}} \quad (1)$$

MID-infrared is a normalized difference index between TM5 and TM7 shortwave infrared bands. The index is applied over the bare soil of the selected images. After masking the vegetation zones, only 100 samples (55 in irrigated zone and 45 in non-irrigated zones) were selected, 50 were used calibration and 50 for validation (Fig. 5).

A simple linear regression model was conducted between measured topsoil clay content and the MID index to produce clay content maps at 30 m spatial resolution over the bare soil zones of the four selected images.

Interpolation over the covered soil using ordinary cokriging

The ordinary cokriging (OCK) was applied to predict the clay content information at 100 m spatial resolution by forming the best linear unbiased estimator between variables with minimum prediction variance [Wu et al., 2009]. This technique is expected to improve the spatial interpolation of primary variable (target) by integrating the information carried by secondary variables (covariables) [Reza et al., 2010].

The Ordinary Cokriging approach uses the variogram and cross variogram to describe and evaluate for each variable the spatial continuity of the properties [Veyan et al., 2023] and to examine the spatial interdependence between any two variables [Reza et al., 2010], respectively.

Theoretically, the variogram can be calculated as:

$$\gamma(u) = \frac{1}{2\, n_i(u)} \sum_{\alpha_i=1}^{n_i(u)} [Z_i(u_{\alpha i}) - Z_i(u_{\alpha i} + u)]^2 \quad (2)$$

where: $\gamma(u)$ – represents the variogram for a separation distance (lag) u between two locations $Z_i(u_{\alpha i})$ and $Z_i(u_{\alpha i} + u)$, $n_i(u)$ – the number of pairs separated by u.

While the cross variogram $\gamma ij(u)$ is calculated such as:

$$\gamma_{ij}(u) = \frac{1}{2\, n_i(u)} \sum_{\alpha_i=1}^{n_i(u)} [Z_i(u_{\alpha i}) - Z_i(u_{\alpha i} + u)][Z_i(u_{\alpha i}) - Z_i(u_{\alpha i} + u)] \quad (3)$$

For each data, the experimental variogram was constructed then a theoretical model was fitted to this [Adhikari et al., 2009]. The best fit

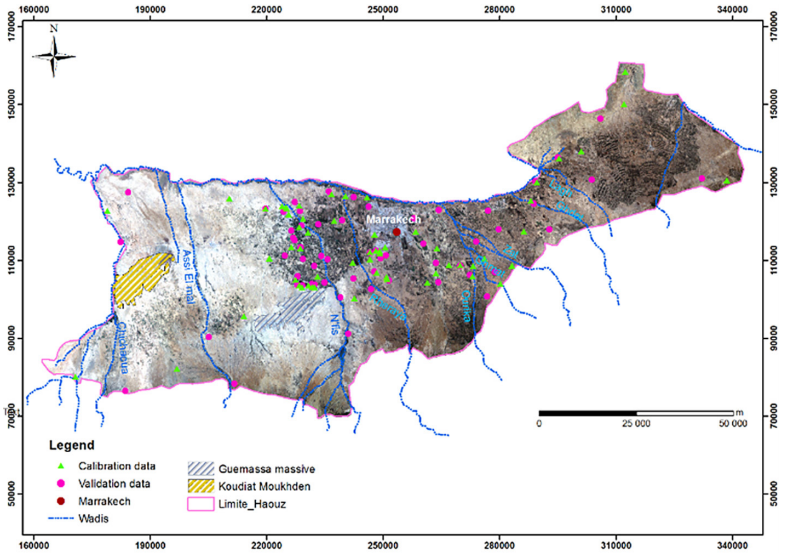

Fig. 5. Location of the calibration and validation samples of soil texture over the Haouz plain

model for those analyzed data was a spherical model, wherein the equation is expressed such as:

$$\begin{cases} \gamma(u) = C_0 + C_1 \left[\frac{3}{2}\left(\frac{u}{a}\right) - \frac{1}{2}\left(\frac{u}{a}\right)^3 \right] \text{u} \le \text{a} & (4) \\ \gamma(u) = C_0 + C_1 \ \text{u} > \text{a} & (5) \end{cases}$$

where: α – the range, C_0 – the nugget semi-variance and C_{0+} C_1 is the sill.

To see the relative contribution of nugget to the total variance, we calculated the relative nugget effect (RNE) according to:

$$RNE = \left(\frac{C_0}{C_0 + C_1}\right) * 100 \quad (6)$$

To interpolate the clay content at unsampled location using Ordinary Cokriging we use the variogram parameters extracted for each fitted model. The ordinary cokriging estimator with the associated variance can be represented as in equations (7) and (8), respectively.

$$Z_{OCK}^{(1)}(u) = \sum_{i=1}^{N_v} \sum_{\alpha_i=1}^{n_i(u)} \lambda_{\alpha_i}^{OCK}(u) Z_i\ (u_{\alpha_i}) \quad (7)$$

$$\sigma_{OCK}^2(u) = C_{ll}(0) - \mu_l^{OCK}(u) - \\ - \sum_{i=1}^{N_v} \sum_{\alpha_i=1}^{n_i(u)} \lambda_{\alpha_I}^{OCK}(u)\, C_{il}(u_{\alpha_i} - u) \quad (8)$$

where: N_v – the number of variables Z_i, $\lambda_{\alpha_I}^{OCK}$ – represents data weights, μ_l^{OCK} – the Lagrange multiplier of the cokriging system and ($u_{\alpha i}$–u) denotes the distance between $u_{\alpha i}$ and u.

The geostatistical computations and spatial analysis were performed in a GIS environment, using the geostatistical wizard.

The predicted topsoil clay content was compared to the on 50 field samples dedicated to the validation process. The determination coefficient (R^2) (Eq. 9) and the Root Mean Square Error (RMSE) (Eq. 10) were used to evaluate the performance of the prediction models [Martin et al., 2020]. The first one measure the effectiveness of a variable to predict another variable, and the second one measures the discrepancy of predicts values around observed ones [Dulakshi, 2022]

$$R^2 = \frac{\sum_{i=1}^{n}(Z^*(x_i) - \bar{Z})^2}{\sum_{i=1}^{n}(Z(x_i) - \bar{Z})^2} \quad (9)$$

$$RMSE = \sqrt{\frac{1}{n}\sum_{i=1}^{n}(Z(x_i) - Z^*(x_i))^2} \quad (10)$$

where: $Z(x_i)$ and $Z^*(x_i)$ – the observed and the predicted value of clay content, respectively and n is the number of observations.

Estimation and validation of the soil hydraulic properties

The clay content information was used to derive the soil moisture at field capacity (θ_{fc}), the wilting point (θ_{wp}) and the saturated conductivity hydraulic (K_{sat}) at 100 m spatial resolution in the Haouz plain, by applying different pedotransfer functions (PTFs) that are based only on clay content.

The soil moisture at field capacity (θ_{fc}) is derived from evaporation models proposed by Noilhan and Mahfouf (1996) and successfully tested for more than 30 sites around the world by Merlin et al. (2016). θ_{ffc} for each pixel is estimated as:

$$\theta_{fc} = 0.089 * (100 * f_{clay})^{0.3496} = 0.445 * f_{clay}{}^{0.3496} \quad (11)$$

Previous works in the Houz plain have derived θ_{fc} and θ_{wp} from Beerkan tests [Benabdelouahab, 2005; Boulet et al., 2009] as follows:

$$\theta_{fc} = 0.0086 * f_{clay} + 0.0756 \quad (12)$$

$$\theta_{\text{wp}} = 0.0076 * f_{clay} - 0.0035 \quad (13)$$

Reichert et al. (2009) expressed the relation between the clay content and the soil moisture at wilting point as follows:

$$\theta_{\text{wp}} = 0.037 * f_{clay}{}^{0.51} \quad (14)$$

Finally, Diallo and Mariko (2013) proposed the formula describing the relation between field capacity and wilting point in clayey soil as:

$$\frac{\theta_{fc}}{\theta_{wp}} = 1.6 \quad (15)$$

This relationship will be used to test the reliability of obtained maps of $\boldsymbol{\theta}_{fc}$ and $\boldsymbol{\theta}_{wp}$. Puckett et al. (1985) and Kar et al (2004) expressed the relation between the clay content and the saturated conductivity hydraulic (K_{sat}) as follow:

$$K_{sat} = 156.96\ exp(0 - 0.1975 * f_{clay}) \quad (16)$$

where: f_{clay} – the clay fraction (%).

The calculation of θ_{fc} and θ_{wp} makes it possible to estimate the total available water (TAW) which is defined as the capacity of a soil to retain water available to plants which plays an important role for irrigation management. This parameter is estimated as the difference between (θ_{fc}) and (θ_{wp}) as mentioned in [Kirkham, 1972]:

$$TAW = 1000 * (\theta_{fc} - \theta_{wp}) \quad (17)$$

To validate the prediction of θ_{fc}, θ_{wp} and K_{sat}, and to check the accuracy of the applied formulas, two different datasets of test fields were used

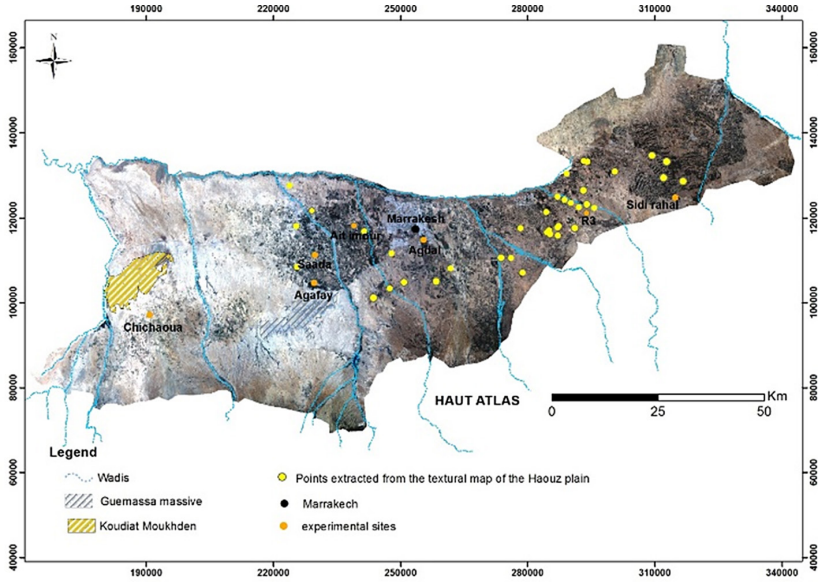

Fig. 6. Location of validation points the hydrodynamic properties of the soil

(Fig. 6). The first one corresponds to a soil sampling on the experiment sites of Chichaoua, Aitimour, Saada, Agafay, Agdal, R3 and Sidi Rahal (Fig. 1). The information on θ_{fc} and θ_{wp} is obtained based on the pedotransfer function of Wosten et al. (2001) [Er-Raki et al., 2007, 2010; Khabba et al., 2013; Nassah et al., 2017]. While the second datasets were used by extracting 38 points from the textural map of the plain of Haouz (Fig. 3), whose textural class of each point is derived from the hydrodynamic properties of the soil by using FAO-56 which describes the physical characteristics of the soil for various soil type [Dirk et al., 2012].

RESULTS AND DISCUSSION

Soil classification using clay content of the soil samples

The sampled textures in the non-irrigated zones consist of high sand fractions (35–85%), moderate clay fraction (25–60%) and low silt fractions (15–40%); the dominant soil type is sandy loam (SaLo). In the irrigated zones the sampled textures consist of high silt fractions (40–60%), lower clay fractions (20–40) and a wide range of sand fractions (0–80%); the dominant soil types

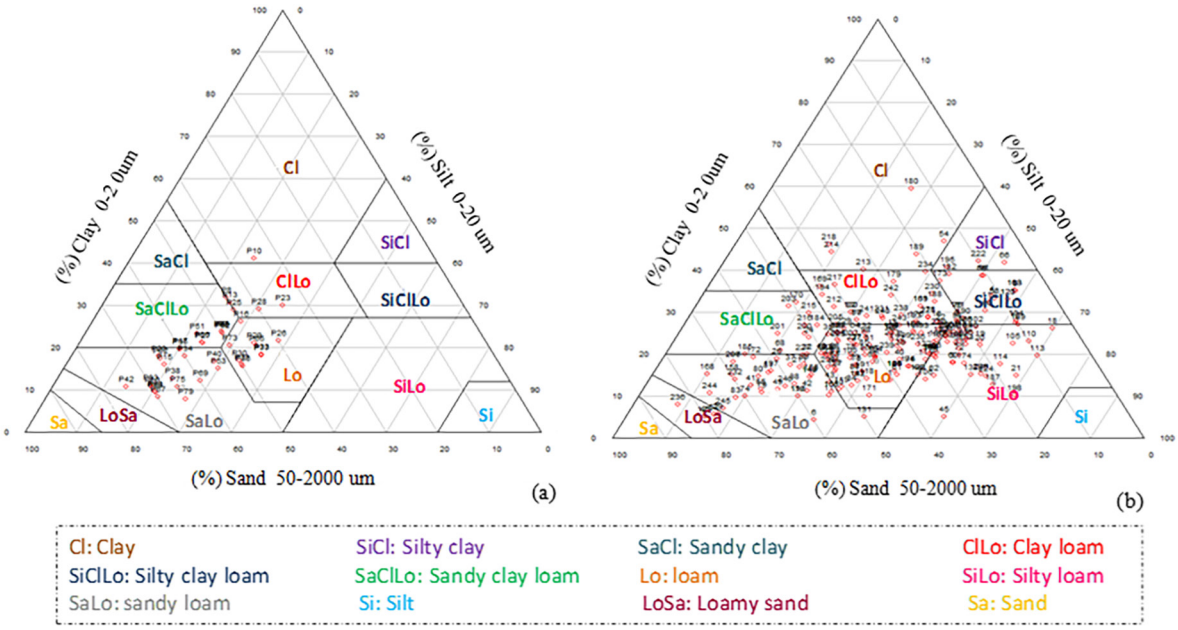

Fig. 7. The categorical distribution of the 200 soil samples in (a) the non-irrigated zones and (b) the irrigated zones of the Haouz plain, according to the USDA textural classes

are silty clay loam (SiClLo), loam (Lo) and clay loam (ClLo).

Clay content maps over bare soil using the MID index

The MID index is extracted on a 3×3 windows (90×90m) corresponding to the 50 selected samples for each of the four selected images (22 June 2013, 08 July 2013, 24 July 2013 and 09 August 2013). There is a positive correlation between the MID index and the clay content, with significant coefficients of determination (R^2) of 0.41, 0.63, 0.56 and 0.72 (Fig. 8). The best correlation (R^2 = 0.72) is obtained for the image of 09 August 2013, according to the following relationship: clay content = 380.8 MID-infrared + 5.90. The other images could be affected by the presence of few crops residue, especially in June 2013 that coincided with the harvest period of wheat.

The obtained relationships between the MID-infrared index and the topsoil clay content are then used to produce the clay content maps at 30 m spatial resolution over bare soil (Fig. 9). The clay content varies from 5 to 40%.

Clay content prediction over the covered soil

The values of clay content obtained for the bare soil at 30 m of spatial resolution were extended to the covered zones using the ordinary cokriging to elaborate the clay content maps at 100 m resolution.

To calculate the variogram, we apply the relationship of 09 August 2013 as primary variable and those achieved for 24 July 2013, 08 July 2013 and 22 June 2013 as secondary variables. The obtained variogram and cross variograms of clay content are well fitted by spherical model (Fig. 10), which corresponds to the best geostatistical model recording the highest R^2 values of about 0.79 (Table 1). In this fitting procedure, the range is 69588 m and the relative nugget effect (RNE) of the variogram is 28.9%, while of the cross variograms are 41.4%, 33.4% and 33.1%, respectively (Table 1).

The interpolated data were validated using the 50 validation soil samples by comparing with the observed topsoil clay content. The obtained results recorded a strong correlation R^2 (0.70) with an RMSE equal to 3.5% (Fig. 11), attesting

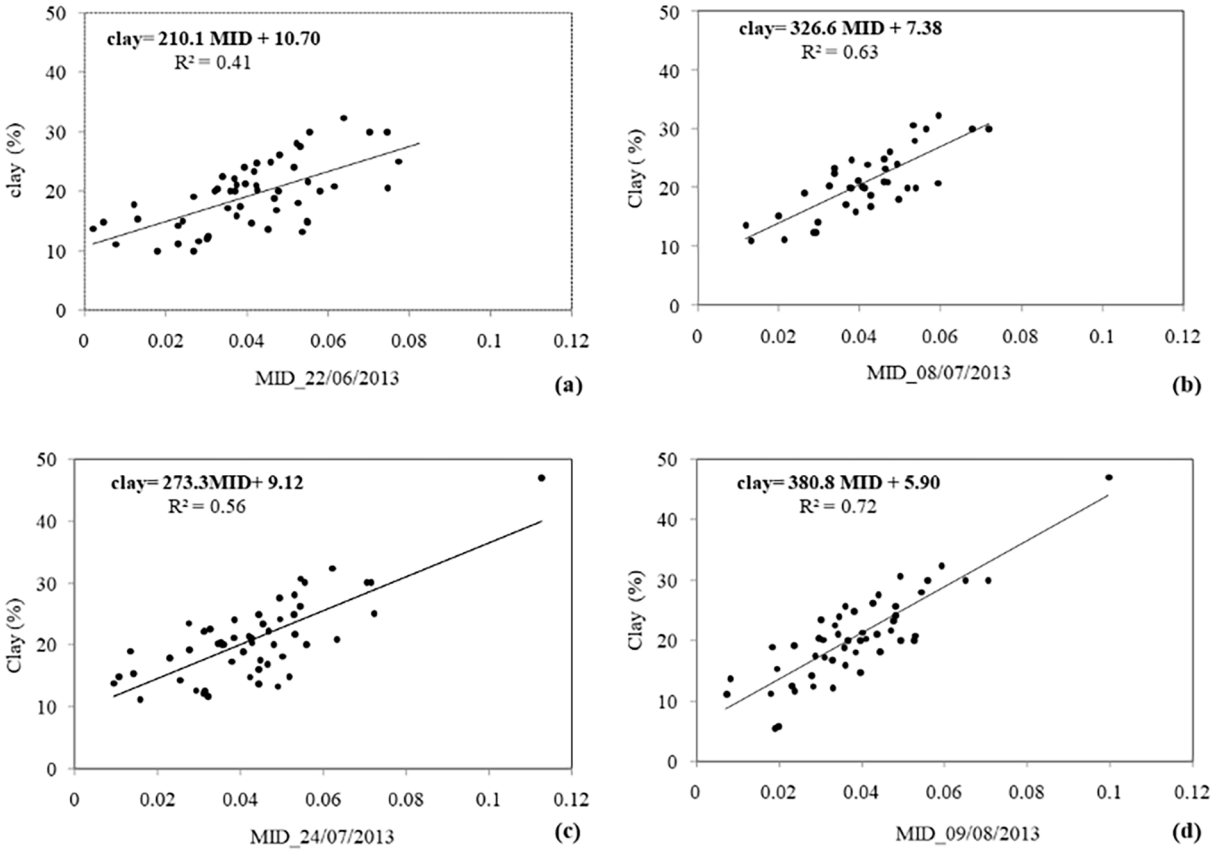

Fig. 8. Linear relationship between MID-infrared index and observed clay content: (a) 22 June 2013, (b) 08 July 2013, (c) 24 July 2013 and (d) 09 August 2013

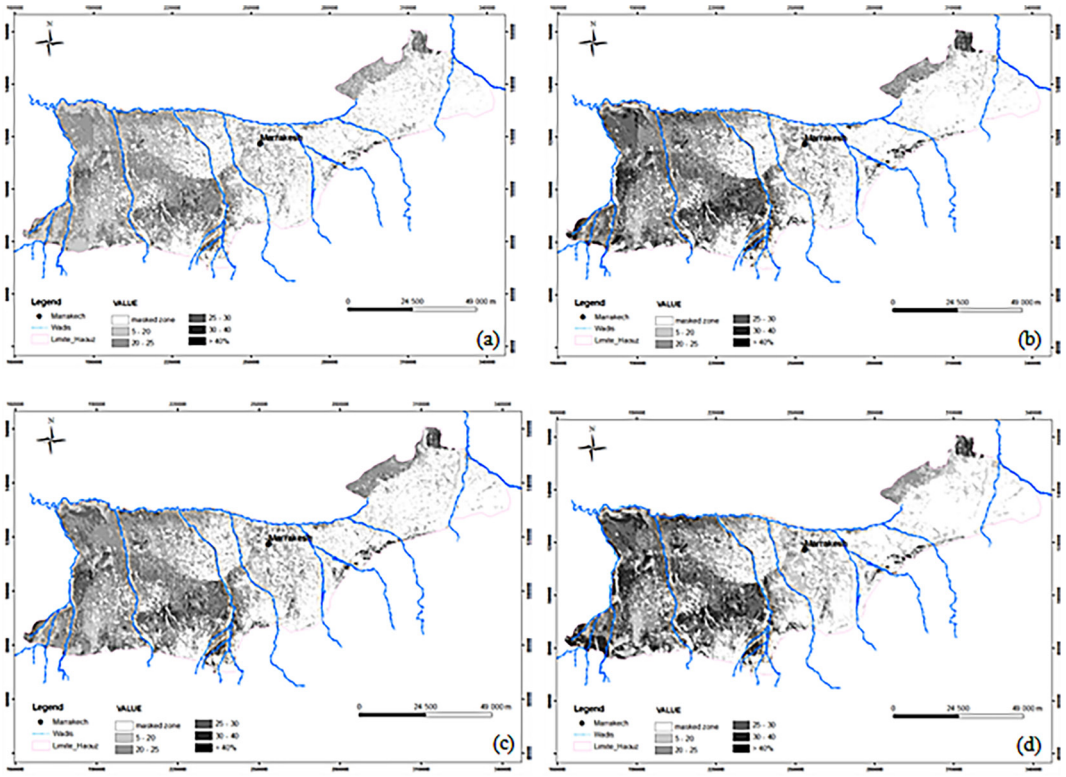

Fig. 9. Clay content maps at 30 m spatial resolution inferred from MID index for (a) 22 June 2013, (b) 08 July 2013, (c) 24 July 2013 and (d) 09 August 2013. The grey pixels correspond to the clay content values, the white one corresponds to the masked zones

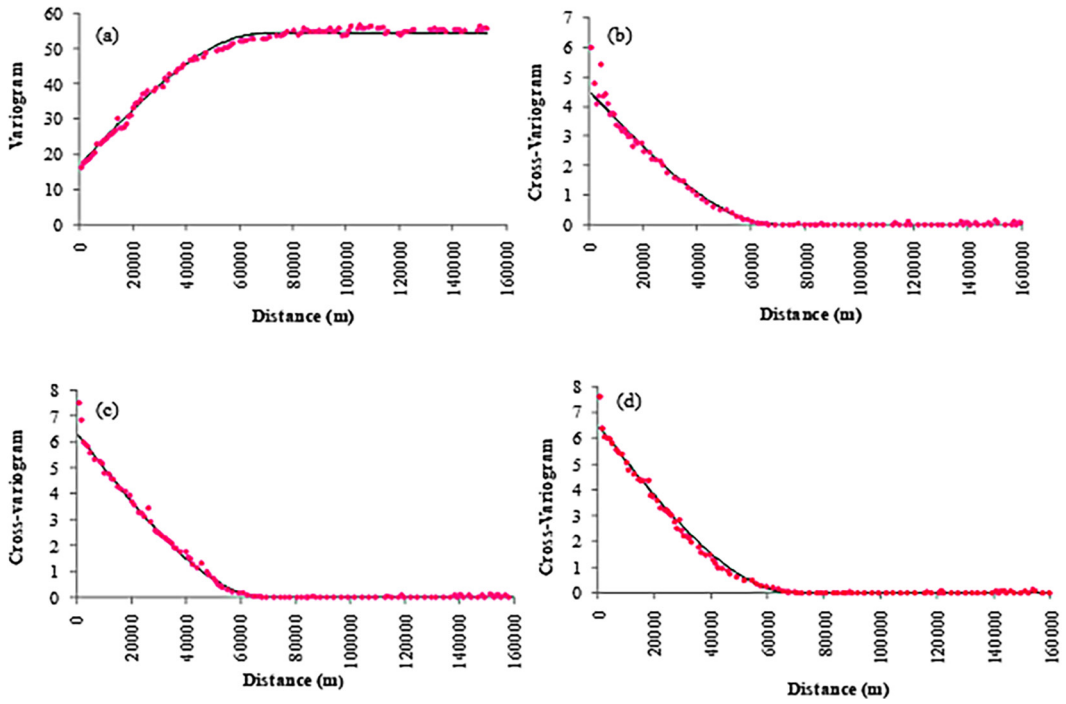

Fig. 10. (a) Experimental variogram and (b-c-d) cross variograms of topsoil clay content over Haouz plain

for a good prediction of the soil content in the plain. The RMSE is lower than the value of 10% obtained by Shabou et al. (2015) in the Kairouan plain in Central Tunisia using the same approach, and Gomez et al. (2012) in the southern part of the La Peyne catchment (43°29′ N and 3°22′ E) 60 km west of Montpellier, France using hyperspectral data.

The predicted topsoil clay content map at 100 m spatial resolution (Fig. 12) shows six classes of clay content according to the USDA texture, varying from 5 to 50%. The entire Haouz plain is characterized by moderate percentage of clay content varying from 20 to 30% (Fig. 12, 13).

Low clay content (5–15%) soils follow the wadis of Ghdat, Zat, Ghmat, Ourika and Rheraya. This could be explained by the nature of the stream sediment materials characterized by coarse textures [Cochet et al., 1998]. The zones with a moderate clay content (20–30%) correspond to the central and northeast of the Haouz plain. The highest clay content (>30%) appears in the eastern part of plain (Tassaout), in the piedmont of the High Atlas, and the western part of the plain along the Chichaoua wadi. This might be inherited from clay and marls material largely present around the plain.

Mapping of derived soil hydraulic properties

The maps of the soil moisture at field capacity (θ_{fc}) and wilting point (θ_{wp}) at 100 m spatial resolution over the Haouz plain (Fig. 14, 15) were derived from the map of clay content by using the different pedotransfer functions (PTFs), (Eqs. 11 to 14). θ_{fc} varies from 0.16 to 0.35 (mm^3/mm^3) based on the PTFs of Noilhan and Mahfouf (1996) (Fig. 14a) and from 0.12 to 0.51 (mm^3/mm^3) using the one derived from the Beerkan test [Benabdelouahab, 2005] (Fig. 14b). θ_{wp} varies from 0.03 to 0.38 (mm^3/mm^3) by using the Eq.13 (Fig. 15a), and from 0.08 to 0.27 (mm^3/mm^3) using Eq.14 (Fig. 15b). The variation of θ_{fc} and θ_{wp} over the plain is related to the clay content. The low values of θ_{fc} and θ_{wp} are extended along the streambeds, and the high values in the eastern part of Haouz plain (Tassaout).

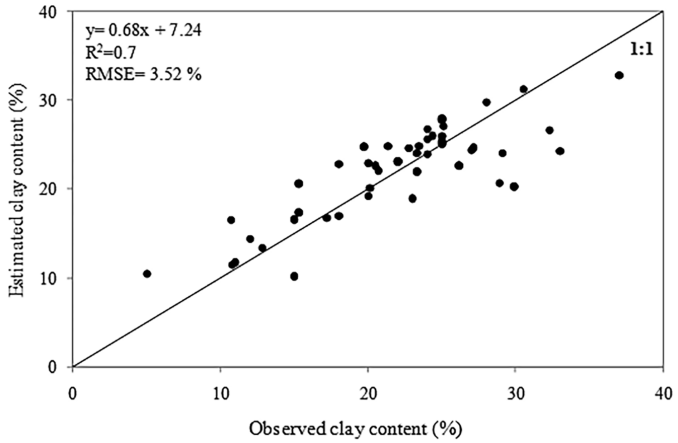

Fig. 11. Comparison between estimated clay content by using the ordinary cokriging with the observed topsoil clay content at 50 independent sampling points

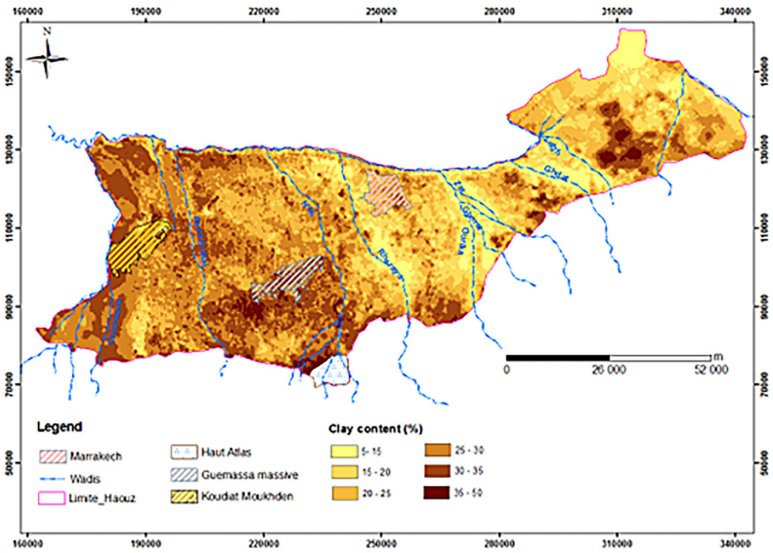

Fig. 12. The spatial distribution of topsoil clay content at 100 m spatial resolution generated using the ordinary cokriging approach

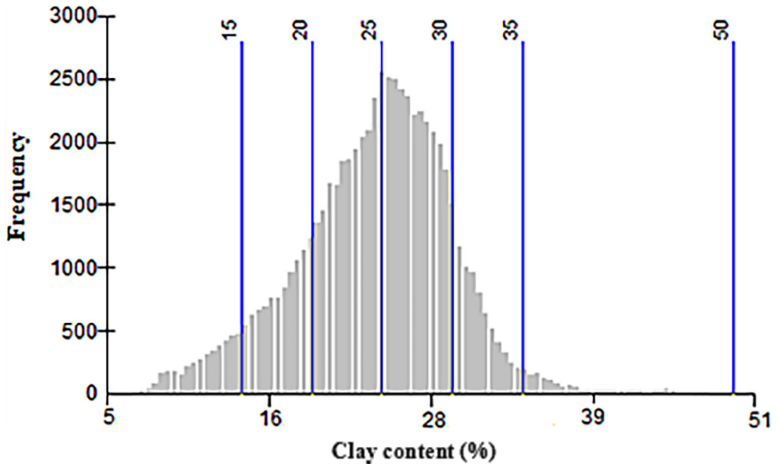

Fig. 13. Frequency distribution of clay content (%) in the Haouz plain

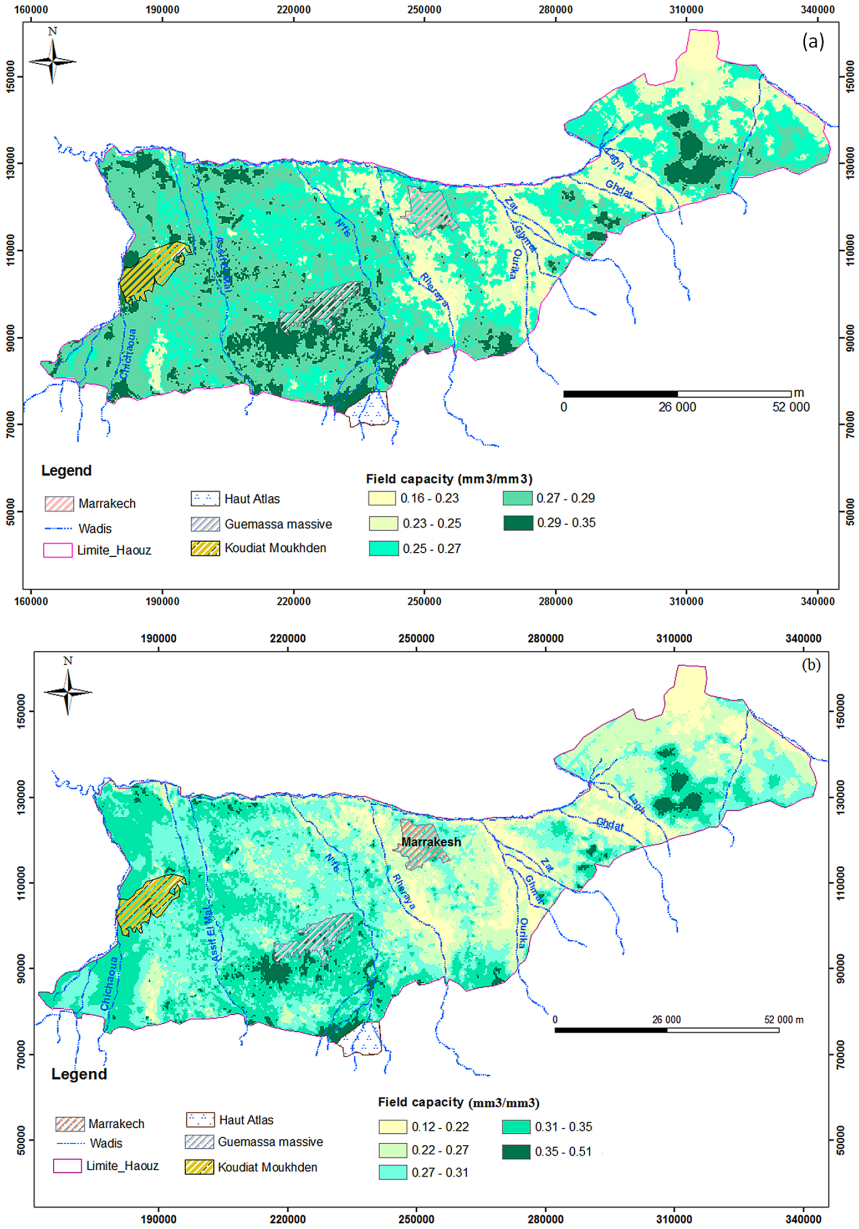

Fig. 14. The spatial variation of moisture soil at Field capacity (θ_{fc}) (Eq. 12): a) and (Eq. 11): b) over Haouz plain at 100 m spatial resolution

The map of the saturated hydraulic conductivity, which is calculated with (Eq. 15) shows a large variation, from 0.14 to 1300 (mm/day) (Fig. 16). Since K_{sat} depends essentially on pore size related to the soil texture [Haghnazari et al., 2015; Eck et al., 2016], therefore the high values of K_{sat} are recorded for coarse textured soils unlike clay and silty clay soils where the K_{sat} values are low.

Figure 17 presents the validation results of θ_{fc}, θ_{wp} and K_{sat}. The results showed that the prediction of θ_{fc}, θ_{wp} over Haouz plain using the (Eq. 12) and (Eq. 14) is considered reasonable (R^2 = 0.75 and 0.8, RMSE = 0.035 and 0.043 mm^3/mm^3 respectively). The results also showed that those PTFs are more suitable for our study area compared to the equations derived from the Beerkan test (Eq. 11 and Eq. 13). Furthermore, the (Eq.15) is suitable for our study area to predict K_{sat} (R^2 = 0.9 and RMSE = 88.8 mm/day).

Diallo and Mariko (2013) stated that a ratio between θ_{fc} and θ_{wp} for a clayey soil equals 1.6. This value is higher compared to our case study with values from 1.39 to 1.44. This underestimation is explained by the fact that the Haouz plain is characterized by a large distribution of moderate clay content class and a small extent of clayey soils.

Using the values θ_{fc} (Eq. 12) and θ_{wp} (Eq. 14), we calculated the plant available water (TAW) based on Eq. 17. The resulting map (Fig. 18) shows values between 121 and 135 (mm/mm) with a high frequency ranged from 132 to 134 (mm). This range is appropriate for soils

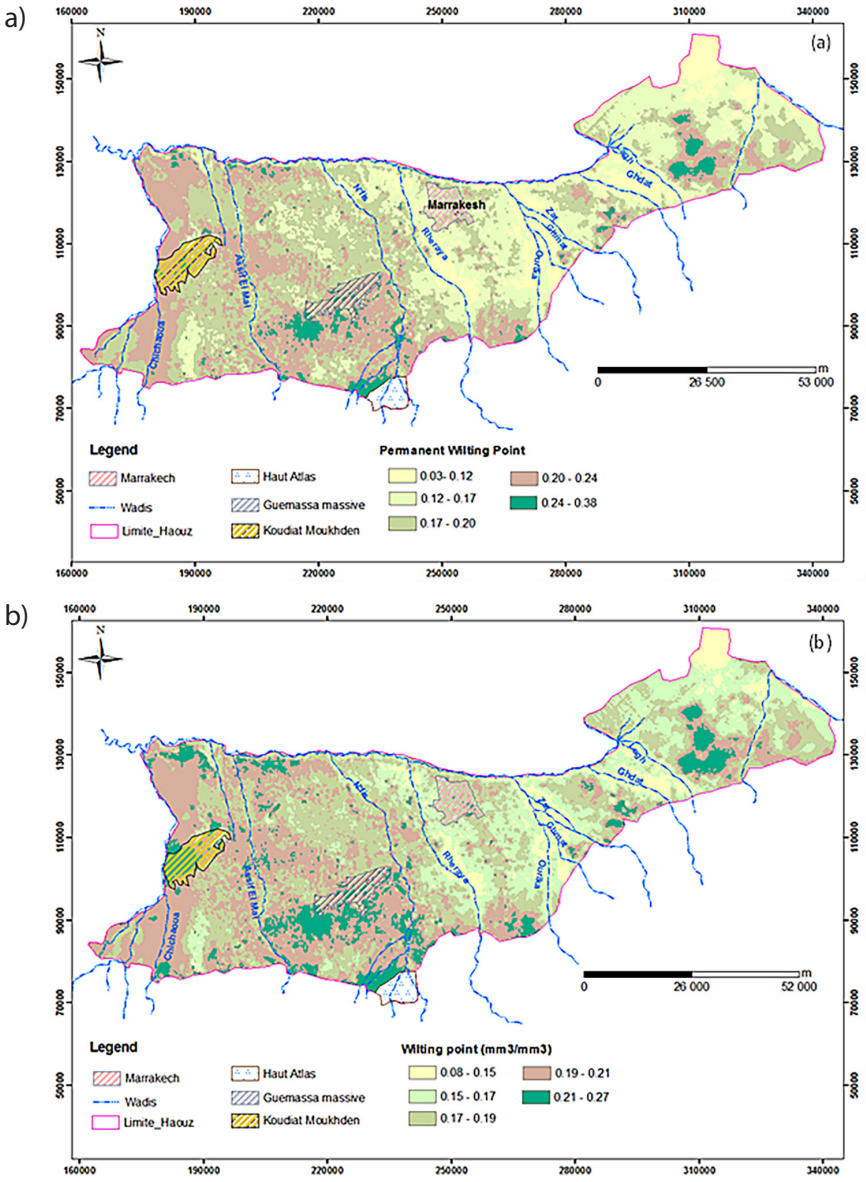

Fig. 15. The spatial variation of moisture soil at (Wilting point (θ_{wp}) (Eq. 13): a) and (Eq. 14): b) over Haouz plain at 100 m spatial resolution

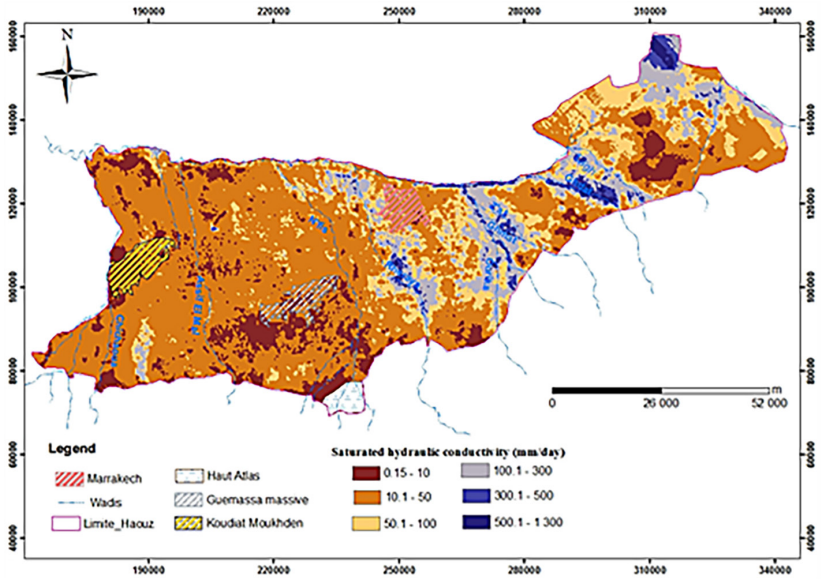

Fig. 16. The spatial variation of saturated hydraulic conductivity

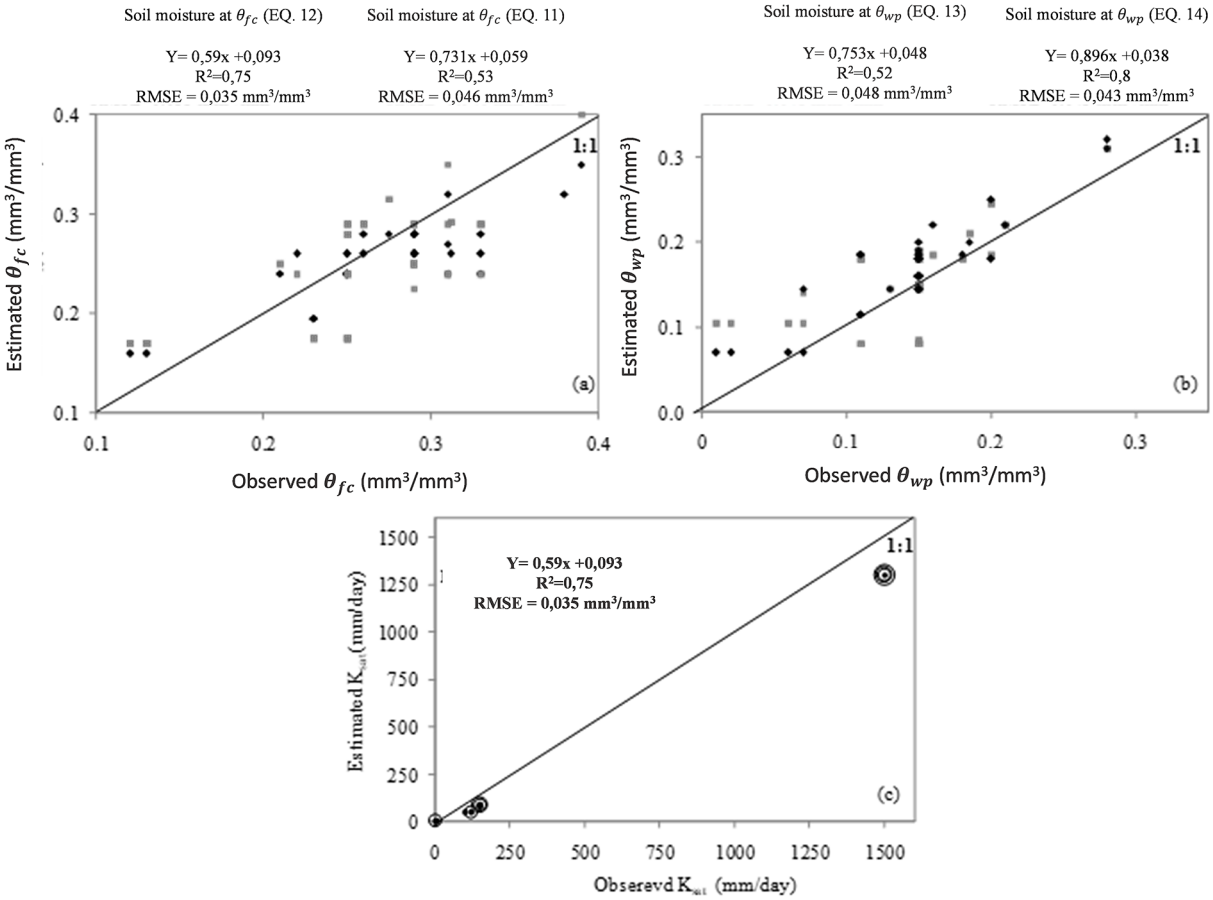

Fig. 17. Validation of both predicted soil moisture: (a) at field capacity, (b) at wilting point, and (c) saturated hydraulic conductivity over 15 test fields

with moderate texture as mentioned in Kirkham, (1972); Allen et al. (2005) also stated that the TAW depends greatly on the soil texture and the TAW values ranged from 132 to 134 correspond to medium texture soil.

CONCLUSIONS

The present study used remote sensing data, Landsat-8 Operational Land Imagery (OLI), for mapping topsoil clay content over the agricultural

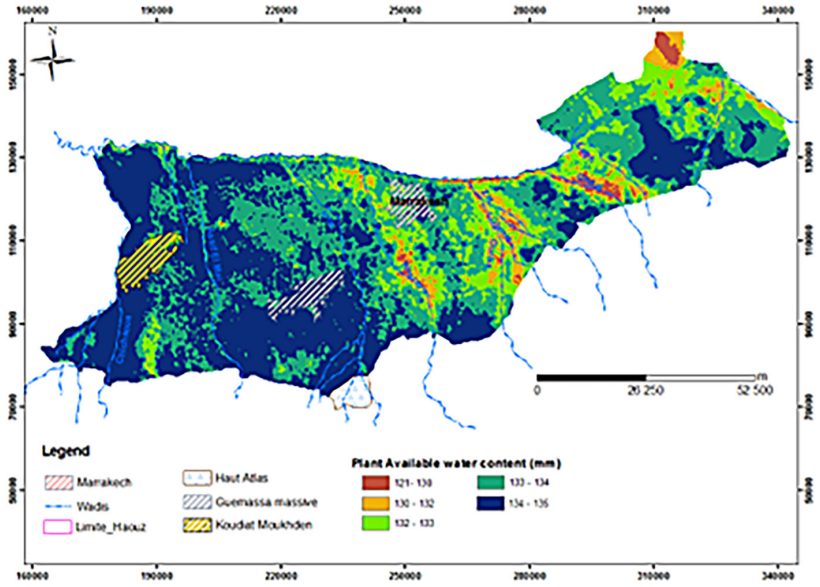

Fig. 18. The spatial variation of total available water (TAW) over the Haouz plain at 100 m spatial resolution

Haouz plain. The obtained map was used to derive soil hydraulic properties such as soil moisture at field capacity (θ_{fc}), wilting point (θ_{wp}) and saturated hydraulic conductivity (K_{sat}).

The results have shown that topsoil clay content over bare soil zones is positively correlated with MID infrared index ($R^2 = 0.72$). This relationship allowed predicting clay content over the bare soil zones. For zones covered by green vegetation and crop residues, where the MID index is not applicable, the ordinary cokriging was used to estimate clay content distribution. The final map of clay content at 100 m resolution is characterized by the high frequency of moderate clay content. It was validated with independent soil samples ($R^2 = 0.70$ and RMSE = 3.5%). This map was converted into soil hydraulic properties based on pedotransfer functions. The obtained maps can be used as input data to hydrological and ecological modeling for agricultural and environmental management.

Acknowledgments

This research was conducted within the Joint International Laboratory-TREMA (https://www.lmitrema.ma/). It was supported by the projects: SAGESSE PPR/2015/48 "Système d'Aide à la décision pour la GEstion des reSSources en Eau", ERANETMED3-062 CHAAMS "global CHange: Assessment and Adaptation to Mediterranean region water Scarcity", ACCWA-823965/H2020-MSCA-RISE-2018 "Accounting for Climate Change in Water and Agriculture management", PRIMA-ALTOS "Managing water resources within Mediterranean agrosystems by Accounting for spatiaL sTructures and cOnnectivitieS" and PRIMA-IDEWA "Irrigation and Drainage monitoring by remote sensing for Ecosystems and Water resources management".

REFERENCES

1. Anderson M.C. 2008. A thermal-based remote sensing technique for routine mapping of land-surface carbon, water and energy fluxes from field to regional scales. Remote Sensing of Environment, 112, 4227–4241.
2. Bartholomeus H., Epema G., Schaepman M. 2007. Determining iron content in Mediterranean soils in partly vegetated areas, using spectral reflectance and imaging spectroscopy. International journal applied earth observation and geoinformation, 9, 194–203.
3. Bastiaanssen W.G.M. 2005. SEBAL model with remotely sensed data to improve water resources management under actual field conditions. Journal of Irrigation and Drainage Engineering, 131(1), 85–93.
4. Benabdelouahab T. 2005. Spatialization of old and recent pedological data with a view to estimating the hydrodynamic parameters of the soils of the Tensift plain. End of engineering studies internship report, Hassan II Agronomic and Veterinary Institute, Rabat, Morocco, pp. 89.
5. Blanco-Canqui, H., Lal R. 2008. Principles of soil conservation and management. Springer, New York, pp. 617.

6. Boukhari, K., Fakir, Y., Stigter, T.Y., Hajhouji, Y., Boulet, G. 2015. Origin of recharge and salinity and their role on management issues of a large alluvial aquifer system in the semi-arid Haouz plain, Morocco. Environmental Earth Sciences, 73(10), 6195–6212.
7. Boulet, G., Mougenot, B., Ben Abdelouahab, T. 2009. An evaporation test based on Thermal Infra Red remote sensing to select appropriate soil hydraulic properties. Journal of Hydrology, 376, 589–598.
8. Camacho-Tamayo, J.H., Rubiano, S.Y., Hurtado, S.M.P. 2014. Near-infrared (NIR) diffuse reflectance spectroscopy for the prediction of carbon and nitrogen in an Oxisol. Agr. Col. 32(1), 86–94.
9. Chehbouni, A., Escadafal, R., Duchemin, B., Boulet, G. 2012. An integrated modeling and remote sensing approach for hydrological study in arid and semi-arid regions: the SUDMED programme. International Journal Remote Sensing, 29(17–18), 5161–5181.
10. Diallo, D., Mariko, A. 2013. Field capacity (FC) and permanent wilty point (PWP) of clay soils developed on Quaternary alluvium in Niger River loop (Mali). International Journal of Engineering Research and Applications, 3(1), 1085–1089.
11. Dirk, R.D., Paquale, S.P., Hsiao, T.C., Fereres, E. 2012. With contributions of the AquaCrop Network.
12. Dulakshi, S.K.K. 2022. Root mean square error or mean absolute error? Use their ratio as well. Information Sciences, 585, 609–629
13. Eck, D.V., Qin, M., Hirmas, D.R., Giménez, D., Brunsell, A. 2016. Relating Quantitative Soil Structure Metrics to Saturated Hydraulic Conductivity. Soil Science Society of America, 15, 1.
14. Er-Raki, S., Chehbouni, A., Boulet, G., Williams, D.G. 2010. Using the dual approach of FAO-56 for partitioning ET into soil and plant components for olive orchards in a semi-arid region. Agricultural Water Management, 97, 1769–1778.
15. Er-Raki, S., Chehbouni, A., Guemouria, N., Duchemin, B., Ezzahar, J., Hadria, R. 2007. Combining FAO-56 model and ground-based remote sensing to estimate water consumptions of wheat crops in a semi-arid region. Agricultural water management, 87(1), 41–54.
16. Giarola, N.F.B., Silva, A.P., Imhoff, S. 2002. 'Relações entre propriedades físicase características de solos da Região Sul do Brasil'. Revista Brasileira de Ciencia do Solo, 26, 885–893.
17. Gomez, C., Lagacherie, P., Coulouma, G. 2012. Regional predictions of eight common soil properties and their spatial structures from hyperspectral Vis–NIR data'. Geoderma. 189–190, 176–185.
18. Greve, M.H., Kheir, R.B., Greve, M.B., Bocher, P.K. 2012. Quantifying the ability of environmental parameters to predict soil texture fractions using regression-tree model with GIS and LIDAR data: The case study of Denmark. Ecological Indicators, 18, 1–10.
19. Haghnazari, F., Shahgholi, H., Feizi, M. 2015. Factors affecting the infiltration of agricultural soils: review. International Journal of Agronomy and Agricultural Research, 6(5), 21–35.
20. Hagolle, O., Huc, M., Pascual, D.V., Dedieu, G.A. 2010. multi-temporal method for cloud detection, applied to Formosat-2, Venμs, Landsat and Sentinel-2 images. Remote sensing environment, 114, 1747–1755.
21. Heuvelink, G.B.M., Kros, J., Reinds, G. J., De Vries, W. 2016. Geostatistical prediction and simulation of European soil property maps. Geoderma Regional, 7, 201–215.
22. Kaihua, L., Shaohui, Xu., Jichun, Wu., Qing, Z. 2013. Spatial estimation of surface soil texture using remote sensing data, Soil Science and Plant Nutrition, 59(4), 488–500.
23. Kar, G., Singh, R., Verma, H.N. 2004. Spatial variability studies of soil hydro-physical properties using GIS for sustainable crop planning of a watershed of eastern India and its testing in a rainfed rice area, Australian Journal of Soil Research, 42(4), 369–379
24. Khabba, S., Jarlan, L., Er-Raki, S., Le Page, M., Ezzahar, J., Boulet, G., Simonneaux, V., Kharrou, H., Hanich, L., Chehbouni, G. 2013. The SudMed program and the Joint International Laboratory TREMA: A decade of water transfer study in the Soil-Plant-Atmosphere system over irrigated crops in semi-arid area. Procedia Environmental Sciences, 19, 524–533.
25. Kirkham, D., Powers, W. L., John, W., Sons, New York, NY, 1972.
26. Lal, R., Stewart, B.A. 2013. Soil management for sustaining ecosystem services. Advances in Soil Science, CRC Press, Boca Raton, Florida, USA, 521–536.
27. Martin, Ć., Shady, H.E.A.A., Ahmed, F.Z. 2020. On the root mean square error (RMSE) calculation for parameter estimation of photovoltaic models: A novel exact analytical solution based on Lambert *W* function. Energy Conversion and Management, 210, 112716.
28. Merlin, O., Stefan, V.G., Amazirh, A., Chanzy, A., Ceschia, E., Er Raki, S., Gentine, P., Tallec, T., Ezzahar, J., Bircher, S., Beringer, J., Khabba, S. 2016. Modeling soil evaporation efficiency in a range of soil and atmospheric conditions using a meta-analysis approach, Water Resources Research, 52, 3663–3684.
29. Mulder, V.L., De Bruin, S., Schaepman, M.E., Mayr, T.R. 2011. The use of remote sensing in soil and terrain mapping-A review, Geoderma, 162, 1–19.
30. Muller E., Décamps, H. 2000. Modeling soil moisture reflectance. Remote sensing of environment.

76, 173–180.

31. Nassah, H., Er-Raki, S., Khabba, S., Fakir, Y., Raibi, F., Merlin O, Mougenot, B. 2017. Evaluation and analysis of deep percolation losses of drip irrigated citrus crops under non-saline and saline conditions in a semi-arid area. Biosystems Engineering: Crop Water Status, 165, 10–24.
32. Nielsen, D., Wendroth, O. 2003. Spatial and Temporal statistics-Sampling Field Soils and Their Vegetation. GeoEcology textbook, Catena-Verlag, Reiskirchen, 614.
33. Noilhan, J., Mahfouf, J.F. 1996. The ISBA land surface parameterisation scheme. global planetary change, 13, 145–159.
34. Oliveira, L.B., Riveiro, M.R., Jacomine, P.K.T., Rodrigues, J.J.V., Marques, F.A. 2002. Funções de pedotransferência para predição da umidade retida a potenciais específicos em solos do Estado de Pernambuco. Revista Brasileira de Ciência do Solo, 26, 315–323.
35. Ouerghemmi, W., Gomez, C., Naceur, S., Lagacherie, P. 2011. Applying blind source separation on hyperspectral data for clay content estimation over partially vegetated surfaces. Geoderma, 163, 227–237.
36. Puckett, W.E., Dane, J.H., Hajek, B.F. 1985. Physical and Mineralogical Data to Determine Soil Hydraulic Properties. Soil Science Society of America, 49, 831–836.
37. Reichert, J.M., Albuquerque, J.A., Kaiser, D.R., Reinert, D.J., Urach, F.L., Carlesso, R. 2009. Estimation of water retention and availability in soils of rio grande do sul. Revista Brasileira de Ciência do Solo, 33, 1547–1560.
38. Reza S., Baruah U., Sarkar D., Das T. 2010. Evaluation and comparison of ordinary kriging and inverse distance weighting methods for predication of spatial variability of some chemical parameters of Dhalai district, Tripura.
39. Saxton, K.E., Rawls, W.J. 2006. Soil water characteristic estimates by texture and organic matter for hydrologic solutions. Soil Science Society of America, 70, 1569–1578.
40. Shabou M., Mougenot B., Lili Chabaane Z., Walter C., Boulet G., Ben Aissa N., Zribi, M. 2015. Soil clay content mapping using a time series of Landsat TM data in semi-arid lands. Remote Sensing, 7, 6059–6078.
41. Veyan, F.S., Muntadher, A.S., Qahtan, A.M., Al Nuaimy.2023. Characterization of the Chemical Properties of Deposited Red Clay Soil Using GIS Based Inverse Distance Weighted Method in Kirkuk City, Iraq. Ecological Engineering & Environmental Technology, 24(7), 46–60.
42. Vidhya, L.S., Jijo, J., Soundariya, S., Vishalini, T., Kasinatha Pandian, P. 2015. A Comparison of Soil Texture Distribution and Soil Moisture Mapping of Chennai Coast using Landsat ETM+ and IKONOS Data. Aquatic Procedia, 4, 1452–1460.
43. Vohland, M., Ludwig, M., Thiele-Bruhn, S., Ludwig, B. 2014.Determination of soil properties with visible to nearand mid-infrared spectroscopy: Effects of spectral variable selection. Geoderma, 223–225, 88–96.
44. Wang, D.C., Zhang, G.L., Zhao, M.S., Pan, X.Z., Zhao, Y.G., Li, D.C. 2015. Retrieval and mapping of soil texture based on land surface diurnal temperature range data from MODIS. PLoS ONE, 10(6).
45. Webster, R., Oliver, M.A. 2001. Geostatistics for Environmenntal Scientists. Statistics practice. Willy, Chichester, 265.
46. Wösten, J.H.M., Van genuchten, M.T. 1988. Using texture and other soil properties to predict the unsaturated soil hydraulic functions. Soil Science Society of America Journal, 52, 1762–1770.
47. Wu, C., Wu, J., Luo, Y., Zhang, L., De Gloria, S.D. 2009. Spatial prediction of soil organic matter content using cokriging with remotely sensed data. Soil Science Society of America Journal, 73, 1202–1208.
48. Zeynal, T., Yücel, T., Yahya, U., Abdul, M.M. 2019. Prediction and mapping of soil clay and sand contents using visible and near-infrared spectroscopy. Biosystems Engineering**.** Intelligent Systems for Environmental Applications, 177, 90–100.
49. Zhang, S.W., Shen, C.Y., Chen, X.Y., Ye, H.C., Huang, Y.F., Lai, S. 2013. Spatial interpolation of soil texture using compositional kriging and regression kriging with consideration of the characteristics of compositional data and environment variables. Journal of Integrative Agriculture, 12(9), 1673–1683.